doi:10.1038/nature09514

SUPPLEMENTARY METHODS

Subjects

We used adult (> 120 post hatch days) male zebra finches (*Taeniopygia guttata*) that were either raised in our colony or obtained from an outside breeder (Perfect Birds, Milton, FL). All animal procedures were reviewed and approved by the MIT committee on animal care.

Intracellular recording during singing

Intracellular recordings were achieved in the zebra finch using a custom microdrive constructed out of 3D printed plastic (AP Proto, Inc). A lightweight linear actuator (Smoovy Series 0515, Faulhaber) was used to move the shuttle along its axis, and Teflon screws were used to position and stabilize the micropipette. A small preamplifer was mounted at the base of the device which routed signals to a commercially available intracellular amplifier (Neuro Data, Cygnus Technology, Inc.). The microdrive also incorporated a pair of threaded holes to allow the bird to be temporarily head-fixed during insertion of the recording electrode into the microdrive.

The microdrive was surgically implanted above HVC under isolfurane anesthesia (1-2%). HVC was first localized using antidromic activation from RA. Thus, as a first step, the borders of RA were localized using a carbon-fiber electrode (Kation Scientific) to determine the extent of the characteristic spontaneous activity in RA. Second, a bipolar stimulating electrode (.002 stainless steel or tungsten) was inserted into the center of RA for antidromic stimulation of HVC. A small craniotomy (< 100 μm) was opened over HVC and the location was confirmed by observing antidromic activation from RA. The microdrive was then affixed to the skull with dental acrylic. The craniotomy was covered with a silicone casting compound (KWIK-Cast, WPI). Birds were given analgesics and antibiotics as part of standard

postoperative care procedures. Zebra finches typically resumed singing in response to the presentation of a female bird within 48 hours following surgery.

On each day of recording, animals were head-fixed using the threaded holes on the microdrive. Under a stereomicroscope, the craniotomy was enlarged (200 μm dia), the underlying dura was removed, an electrode pipette was loaded into the microdrive and was lowered into HVC. To protect against desiccation, a silicone fluid (Dow Corning) was introduced to the well surrounding the craniotomy. Once the electrode was lowered into the brain, the bird was released from the head restraint and the microdrive was attached to a thin electrical cable in a cylindrical recording chamber (23cm diameter x 20cm height). The electrode was slowly advanced using the motorized actuator on the microdrive until an increase in electrode impedance was observed. Break-in was achieved with standard electrode 'buzzing' procedures. Once a stable recording was achieved, a female bird was presented to the male to elicit directed singing. Only neurons that had a resting potential less than -60mV and spike height greater than 50mV above rest were analyzed further. Recordings lasted from four minutes to over an hour.

Electrodes could be easily replaced as needed by temporarily holding the bird in a soft foam restraint and head-fixing the bird under the stereomicroscope. The old pipette could then be retracted and removed, and a new pipette loaded. At the end of a day of recording, a small amount of Kwik-Cast (WPI) was applied to the surface of the craniotomy in order to protect the brain overnight. Recordings were attempted for approximately 3-7 days per bird.

Somatic current injection during singing. As a test of the ramp-to-threshold model, in three neurons we were able to examine the effect of somatic current injection on burst timing. One neuron was held long enough to record with injected currents of +0.5 nA, -0.5 nA and -1.0 nA, producing an average membrane potential change of 7.9 mV, -7.8 mV, and -24.2 mV relative to zero holding current, respectively. Two other neurons recorded with -0.5nA hyperpolarizing current (average membrane potential change -10.3 mV).

Intracellular recording in the sleeping bird

To encourage sleeping during daytime hours, birds were housed with a reverse light:dark cycle (12h:12h) for at least a week before surgery. During an initial surgical step, a thin, stainless steel headplate was affixed to the skull with dental acrylic. RA was then localized using a carbon fiber electrode (Kation Scientific) before implantation of the bipolar stimulating electrode (.002 stainless steel or tungsten). The bird was then placed in a form-fitting foam restraint and transferred to the recording site without further isoflurane. Local anesthetic (Lidocaine gel) was intermittently applied to wound margins. In an initial subset of experiments, finches were given a subcutaneous injection of melatonin (1-10 µg in PBS). The neurons recorded in the presence of melatonin (15 of 80 total neurons) exhibited burst rates that did not differ significantly from naturally sleeping animals. As such, these neurons were combined with the remainder of the recorded cells.

Prior to recording, a small (~ 200 µm) craniotomy was made over HVC. Whole-cell recording electrodes (5-8 MΩ) were filled with an internal solution (pH = 7.25, 290-300 mOsm) which contained the following (in mM): 0.2 EGTA, 130 K-Gluconate or K-Methanesulfonate, 4 KCl, 2 NaCl, 10 HEPES, 4 ATP-Mg, 0.3 GTP-Tris, 14 Phosphocreatine-Tris. Using techniques similar to those described elsewhere [46], electrodes were lowered into HVC until a gigaseal could be obtained and a stable whole-cell recording achieved. In some experiments, an injection pipette (20-30 µm opening) was subsequently positioned less than 100 µm from the recording site in order to introduce pharmacological agents to the recorded neuron. Specifically, to examine the role of L-type calcium channels in neuronal bursting, small volumes (5-20 nL) of (+/-)-BAY K 8644 (100µM, A.G. Scientific) or Nifedipine (100µM, Sigma) were injected (Nanoject II, Drummond Scientific). In the results section (and Figure 4h-m), the activity of neurons in the presence of BAY K 8644 and Nifedipine is compared to unmanipulated neurons in which no injection was made (control condition).

Slice recordings

Parasagittal slices (400 µm thickness) were prepared on a vibrating microtome (Leica VT1000) and placed in ice-cold ACSF (sodium replaced with equimolar sucrose). The standard ACSF used consisted

of the following (in mM): 126 NaCl, 3 KCl, 1.25 NaH_2PO_4, 2 $MgSO_4$-$7H_2O$, 26 $NAHCO_3$, 10 Dextrose, 2 $CaCl_2$-$2H_20$. Slices were held in a custom interface-style holding chamber at room temperature until the time of the recording. The slices were recorded at 35 degrees C on a Haas-type commercially available recording chamber system (VT5000, Leica). Blind whole-cell recordings were carried out using procedures similar to those described for the sleeping bird. QX-314 (5 mM) was used in the internal electrode solution in a subset of these experiments.

Antidromic Identification

HVC contains several major neuronal types that can be defined on the basis of their synaptic targets [47,48]. Our experiments and analysis has focused on neurons within HVC that project to RA. All results reported for $HVC_{(RA)}$ neurons in this paper we based on antidromically-identified neurons. We delivered short stimulating pulses to RA (single pulse of 200 μs duration, 20-200 μA) while recording in HVC (Supplementary Figure 1a). Characteristic antidromic responses exhibited short latencies (2-8 ms) and minimum latency variability (< 100 μs), both *in vivo* (Supplementary Figure 1b) and *in vitro* (Supplementary Figure 1c). For *in vitro* experiments, the antidromic stimulating electrodes were placed in RA, since parasaggital slices contain portions of HVC, RA and the HVC-to-RA fiber tract. For experiments in which QX-314 was used to block sodium spikes, the antidromic identification step was performed in cell-attached mode before spiking was blocked by QX-314 upon break-in.

Computational Model

Network model

The model consists of 70 groups, each containing 30 $HVC_{(RA)}$ neurons. The groups are organized in a sequentially connected chain through which activity propagates. Each neuron is connected to a neuron in the next group with a probability P , and connection strength randomly chosen in a range from 0 to $G_{EE,\max}/(30P)$ (Supplementary Fig. 4a). Recurrent inhibitory connections in HVC are modelled by a

population of 300 inhibitory interneurons ($HVC_{(I)}$). An $HVC_{(RA)}$ neuron connects to an $HVC_{(I)}$ neuron with a probability 0.05 and an excitatory synaptic conductance randomly chosen from 0 to $0.5\,mS/cm^2$; an $HVC_{(I)}$ neuron connects to an $HVC_{(RA)}$ neuron with a probability 0.1 and an inhibitory synaptic conductance randomly chosen from 0 to $0.2\,mS/cm^2$. This value was chosen such that spike propagation can be maintained over a wide range of $G_{EE\max}$.

Non-bursting model of $HVC_{(RA)}$ neurons

The non-bursting model of $HVC_{(RA)}$ neurons is implemented in a single compartment containing Na+ and delay-rectified K+ conductance for action potential generation as well as leak conductance [49]. The membrane potential $V(t)$ evolves according to $C_m \frac{dV(t)}{dt} = I_L + I_{Na} + I_{Kdr} + I_{exc} + I_{inh} + \frac{I_{ext}}{A}$, where $C_m = 1\,\mu F/cm^2$ is the membrane capacitance; $I_L = -G_L(V - E_L)$ is the leak current, with leak conductance $G_L = 0.1\,mS/cm^2$ and reversal potential $E_L = -80\,mV$; $I_{Na} = -G_{Na} m_\infty^3 h(V - E_{Na})$ is the Na+ current, with conductance $G_{Na} = 60\,mS/cm^2$, reversal potential $E_{Na} = 55\,mS/cm^2$, Na+ activation function $m_\infty(V) = 1/(1 + \exp(-(V + 30)/9.5))$ and gating variable h; $I_{Kdr} = -G_{Kdr} n^4 (V - E_K)$ is the delay rectified K+ current, with conductance $G_{Kdr} = 8\,mS/cm^2$, reversal potential $E_K = -90\,mV$, and gating variable n; $I_{exc} = -g_{exc}(t)V$ is the excitatory synaptic current, where $g_{exc}(t)$ is the total excitatory synaptic conductance; $I_{inh} = -g_{inh}(t)(V - E_I)$ is the inhibitory synaptic current, where $g_{inh}(t)$ is the total inhibitory conductance and $E_I = -80\,mV$ is the reversal potential; I_{ext} is the external current; and finally, $A = 5000\,\mu m^2$ is the area of the neuron.

Synaptic conductances on the neurons follow "kick-and-decay" kinetics implemented as follows: $g_{exc \text{ or } inh} \rightarrow g_{exc \text{ or } inh} + G$ when a spike arrives at a excitatory or inhibitory synapse with conductance G, and $\tau_{exc \text{ or } inh}\, dg_{exc \text{ or } inh}/dt = -g_{exc \text{ or } inh}$ in between spikes. The synaptic time constants τ_{exc} and τ_{inh} are set to $5\,ms$.

The gating variables h, n are governed by the following equation:

$$\tau_x \frac{dx}{dt} = x_\infty - x,$$

where $x = h, n$. The voltage dependences of the gating variables are:

$$h_\infty = 1/\left(1 + \exp\left((V + 45)/7\right)\right),$$
$$\tau_h = 0.1 + 0.75/\left(1 + \exp\left((V + 40.5)/6\right)\right),$$
$$n_\infty = 1/\left(1 + \exp\left(-(V + 35)/10\right)\right),$$
$$\tau_n = 0.1 + 0.5/\left(1 + \exp\left((V + 27)/15\right)\right).$$

The response of the non-bursting model of $HVC_{(RA)}$ neurons to current injection is shown in Supplemental Fig. 4b.

Model of $HVC_{(I)}$ neurons

An $HVC_{(I)}$ neuron is modelled as a single compartment neuron that contains Na+ and delay-rectified K+ conductance for action potential generation, leak conductance, and high threshold K+ conductance for enhancing fast spike generation. The membrane potential $V(t)$ evolves according to:

$$C_m \frac{dV(t)}{dt} = I_L + I_{Na} + I_{Kdr} + I_{KHT} + I_{exc} + I_{inh}$$

where $C_m = 1\mu F/cm^2$ is the membrane capacitance; $I_L = -G_L\left(V - E_L\right)$ is the leak current, with leak conductance $G_L = 0.1 mS/cm^2$ and reversal potential $E_L = -65 mV$; $I_{Na} = -G_{Na} m^3 h\left(V - E_{Na}\right)$ is the Na+ current, with conductance $G_{Na} = 100\ mS/cm^2$, reversal potential $E_{Na} = 55\ mS/cm^2$, and gating variable m, h; $I_{Kdr} = -G_{Kdr} n^4\left(V - E_K\right)$ is the delay rectified K+ current, with conductance $G_{Kdr} = 20\ mS/cm^2$, reversal potential $E_K = -80 mV$, and gating variable n; $I_{KHT} = -G_{KHT} w\left(V - E_K\right)$ is the high threshold K+ current, with conductance $G_{KHT} = 500\ mS/cm^2$ and gating variable w; $I_{exc} = -g_{exc}(t)V$ is the excitatory synaptic current, where $g_{exc}(t)$ is the total excitatory synaptic

conductance; $I_{inh} = -g_{inh}(t)(V - E_I)$ is the inhibitory synaptic current, where $g_{inh}(t)$ is the total inhibitory conductance and $E_I = -75mV$ is the reversal potential. The dynamics of the excitatory and inhibitory conductance is the same as in the single compartment model of $HVC_{(RA)}$ neuron, except that the time constant of the excitatory conductance τ_{exc} is set to $2ms$.

The gating variables m, h, n are governed by the following equation:

$$\frac{dx}{dt} = \alpha_x(1-x) - \beta_x x,$$

where $x = m, h, n$. The voltage dependences of the gating variables are:

$$\begin{aligned}
\alpha_m &= (V+22)/(1-\exp(-(V+22)/10)),\\
\beta_m &= 40\exp(-(V+47)/18),\\
\alpha_h &= 0.7\exp(-(V+34)/20),\\
\beta_h &= 10/(1+\exp(-(V+4)/10)),\\
\alpha_n &= 0.15(V+15)/(1-\exp(-(V+15)/10)),\\
\beta_m &= 0.2\exp(-(V+25)/80).
\end{aligned}$$

The gating variable w follows $\tau_w \frac{dw}{dt} = w_\infty - w$, where $w_\infty = 1/(1+\exp(-V/5))$, $\tau_w = 1$.

Bursting model of $HVC_{(RA)}$ neuron

The bursting model of $HVC_{(RA)}$ neurons is implemented with two compartments: a somatic compartment and a dendritic compartment. The model of the soma is the same as in the single compartment model. The dendritc compartment contains a leak conductance, a high threshold Ca++ conductance, and a calcium-activated K+ conductance for generation of a calcium spike in the dendrite. The two compartments are connected ohmically. A calcium spike in the dendrite leads to a stereotypical burst of sodium spikes in the soma.

The membrane potentials V_s and V_d of the soma and dendrite obey the following equations:

$$C_m A_s \frac{dV_s(t)}{dt} = A_s\left(I_{s,L} + I_{s,Na} + I_{s,Kdr} + I_{s,exc} + I_{s,inh}\right) + I_{s,ext} + \frac{\left(V_d - V_s\right)}{R_c},$$
$$C_m A_d \frac{dV_d(t)}{dt} = A_d\left(I_{d,L} + I_{d,Ca} + I_{d,CaK} + I_{d,exc} + I_{d,inh}\right) + I_{d,ext} + \frac{\left(V_s - V_d\right)}{R_c},$$

where $A_s = 5000\,\mu m^2$ is the area of the somatic compartment; $I_{s,L}$, $I_{s,Na}$, $I_{s,Kdr}$ are the leak, Na+ and delayed rectify K+ currents, respectively, with the forms and parameters the same as in the single compartment model of HVC$_{(RA)}$ neuron; $I_{s,exc}$ and $I_{s,inh}$ are the excitatory and inhibitory conductance, whose dynamics is the same as in the single compartment model; $I_{s,ext}$ is the external current to the soma; $R_c = 55\,M\Omega$ is the coupling resistance between the two compartments; $A_d = 10000\,\mu m^2$ is the area of the dendritic compartment; $I_{d,L} = -G_{d,L}\left(V_d - E_L\right)$ is the leak current, with leak conductance $G_{d,L} = 0.1\,mS/cm^2$ and reversal potential $E_L = -80\,mV$; $I_{d,Ca} = -G_{Ca} r^2 \left(V_d - E_{Ca}\right)$ is the high threshold Ca++ current, with conductance $G_{Ca} = 55\,mS/cm^2$, reversal potential $E_{Ca} = 120\,mV$, and gating variable r; $I_{d,CaK} = -G_{CaK}\, c/\left(1 + 6/[Ca]\right)\left(V_d - E_K\right)$ is the calcium-dependent K+ current, with conductance $G_{CaK} = 150\,mS/cm^2$, gating variable c, calcium concentration $[Ca]$, and reversal potential $E_K = -90\,mV$; $I_{d,exc}$ and $I_{d,inh}$ are the excitatory and inhibitory synaptic currents, whose dynamics is the same as in the single compartment model; and finally, $I_{d,ext}$ is the external current to the dendritic compartment.

The gating variables r, c follows $\tau_x \frac{dx}{dt} = x_\infty(V) - x$, where $x = r, c$. The voltage dependences of the gating variables are:

$$r_\infty = 1/\left(1 + \exp\left(-\left(V_d + 5\right)/10\right)\right),$$
$$\tau_r = 1;$$
$$c_\infty = 1/\left(1 + \exp\left(-\left(V - 10\right)/7\right)\right),$$
$$\tau_c = 10.$$

The calcium concentration obeys the following equation:

$$\frac{d[Ca]}{dt} = 0.1 I_{d,Ca} - 0.02[Ca].$$

The response of the bursting (two-compartment) model of $HVC_{(RA)}$ neurons to current injection to the soma and dendrite are shown in Supplemental Figure 4c,d.

Inhibitory network and noise fluctuations

Noise fluctuations are introduced into the membrane potentials of both $HVC_{(RA)}$ and $HVC_{(I)}$ neurons. In the single-compartment model, an $HVC_{(RA)}$ neuron receives an excitatory noise spike train and an inhibitory noise spike train, each generated with a Poisson process at a frequency of 100 Hz. At each excitatory noise spike, a synaptic conductance is randomly selected from 0 to $0.027\ mS/cm^2$ and added to the total excitatory conductance, $g_{exc}(t)$, of the neuron. Thus, the noisy input follows kick-and-decay kinetics in the same way that other synaptic inputs do. Likewise, at each inhibitory noise spike, a synaptic conductance is randomly selected from 0 to $0.027\ mS/cm^2$ and added to the total inhibitory synaptic conductance, $g_{inh}(t)$, of the neuron. This leads to a subthreshold fluctuation of the membrane potential of 3 mV root-mean-square (RMS). During sequence generation, this is reduced to 0.17 mV due to the strong inhibition from the $HVC_{(I)}$ neurons. Similarly, an $HVC_{(I)}$ neuron receives excitatory and inhibitory noise spike trains, each with frequency 250 Hz and maximum noise synaptic conductance $0.45\ mS/cm^2$. This leads to spontaneous firing of $HVC_{(I)}$ neurons at about $10\,Hz$.

In the two-compartment bursting model, an $HVC_{(RA)}$ neuron receives inhibitory and excitatory noise spike inputs at both compartments. At the somatic compartment, the spike trains have frequency 100 Hz and maximum conductance $0.035\ mS/cm^2$; and at the dendritic compartment, frequency 100 Hz and maximum conductance $0.045\ mS/cm^2$. This leads to fluctuations of the membrane potentials in both compartments of *3mV RMS*. During the sequence generation, the RMS is reduced to about 1.5mV due to increased inhibition.

Integrate-and-burst neuron model

To show that stereotypical burst is the key feature for the stability and timing precision in the dynamics of the synaptic chain networks, regardless of the details of the biological implementation of the burst generation, we simulated a network with simple single-compartment integrate-and-burst neurons. The membrane potential $V(t)$ follows the following equations:

$$C_m \frac{dV(t)}{dt} = I_L + I_{exc} + I_{inh} + \frac{I_{ext}}{A}$$

where $C_m = 1\mu F/cm^2$ is the membrane capacitance; $I_L = -G_L(V - E_L)$ is the leak current, with conductance $G_L = 0.1mS/cm^2$ and reversal potential $E_L = -80mV$; I_{exc} and I_{inh} are the excitatory and inhibitory synaptic currents as described for the single-compartment HVC$_{(RA)}$ neuron model, I_{ext} is the external current; and $A = 5000\mu m^2$ is the area of the neuron. Parameters were selected so that the integrate-and-burst model has the same membrane time constant as the single-compartment model of HVC$_{(RA)}$ neuron. When the membrane potential reaches a threshold set at $V_{th} = -53mV$, the neuron emits a burst of 5 spikes in a span of 6ms. After the last spike in the burst, the membrane potential is reset to $-80mV$, and is held there for a refractory period of $20ms$. Noisy fluctuations of the membrane potential are induced as in the single-compartment model, and the noise level is the same as for the single-compartment model ($3mV$ RMS). During sequence generation, the noise level is $0.47mV$ RMS. The network structure and synaptic dynamics are the same as with single-compartment HVC$_{(RA)}$ neurons. Because the integrate-and-burst neuron, with the same area and membrane time constant, is more excitable than the Hodgkin-Huxley-based single-compartment model, the excitatory and inhibitory synaptic strengths needed to be reduced to $G_{EE\max} = 1mS/cm^2$ and $G_{IE\max} = 0.1mS/cm^2$ respectively to achieve a propagation speed comparable to the single-compartment model shown in Fig.5.

Integrate-and-burst neuron model

The network performance was quantified using a number of metrics. The unreliability index quantifies th lack of consistency of burst from run to run (if a neuron bursts 50% of runs the index is 1, indicating it is most unreliable; mathematically, the index is defined as the entropy of the burst occurrence across trials normalized to the entropy of the 50% case). The runtime jitter is defined as the coefficient of variation of the first spike times of neurons in the 56th group. Quantitative comparison of the properties of activity propagation in the one- and two-compartment models stated in the results section was made by computin the averages of these properties over 50 runs of the network. We examined networks with connection probabilities of P=0.1, 0.2, 0.5, and 1.0 and connection strengths of $G_{EE\max}$ from 0.2 to 4 mS/cm^2 in intervals of 0.2 mS/cm^2. The reported average of all metrics was computed over networks (in the stated range of parameters) that exhibited stable propagation. For example, for the non-bursting model with P=0.1 (red trace), networks with $G_{EE,\max} < 0.8$ ms/cm^2 did not exhibit stable propagation and were excluded.

The group width is defined as the time span from the first to the last spikes of neurons in the sam group averaged over 50 runs of the network. The group latency (a quantification of propagation speed) is defined as the difference in the spike times of neurons in successive groups (based on the average time of the first spike in the response, averaged over 50 runs of the network). In the single-compartment model, both group width and group latency showed substantial variations during propagation (Supplementary Fig. 5). To quantify these variations in propagation through the network, we computed the standard deviation (SD) of group width and group latency across neuronal groups. For example, the standard deviation of the values of group width, across neuronal groups, for one particular network (e.g. P=0.1, $G_{EE,\max}$ =3 mS/cm^2, dark blue trace, Supp Fig 5a left panel) was used to compute the value of 'group width SD' plotted in Supplementary Fig. 6a (left panel, dark blue trace at a synaptic conductance of 3). The 'group width SD' was computed for networks with different parameters (connection probability P and synaptic conductance $G_{EE,\max}$), and used to construct the traces shown in Supplementary Fig. 6a.

Another feature of interest is the extent to which network performance is sensitive to the parameters of the network. In particular, it can be seen that there is much more variation in network behavior (Supplementary Fig 6) for the non-bursting network than for the bursting network (left vs right panels, respectively). To quantify this difference, we found the standard deviation of each of the metrics shown in Supplementary Fig. 6, computed across different networks, over a range of network connection probabilities (P=0.1, 0.2, 0.5, and 1.0) and synaptic connection strengths. Again, only networks that exhibited stable propagation were included in this analysis.

SUPPLEMENTARY DISCUSSION

The intracellular recordings of $HVC_{(RA)}$ neuron in the singing bird reveal a highly stereotyped pattern of membrane potential fluctuations and a single large postsynaptic potential that immediately precedes the onset of a song-locked burst of spikes. We observe no ramping, rhythmicity, or other slow subthreshold patterning that could contribute to the temporal patterning of $HVC_{(RA)}$ bursts. These findings are consistent with the predictions of a 'chain model' of sequence generation in HVC, and are not consistent with a large class of models in which subthreshold dynamics determine sequential timing.

In addition, an essential feature of models in which subthreshold dynamics control spike timing is that an experimentally imposed hyperpolarization or depolarization should cause a change in spike timing, a prediction not borne out by observations of stable burst timing during somatic current injection in $HVC_{(RA)}$ neurons. Of course, this prediction requires that the burst generation mechanism be sufficiently well electrotonically coupled to the site of current injection (i.e. the soma). While it is difficult to rule out this potential difficulty, a detailed biophysical model of $HVC_{(RA)}$ neurons suggests that, even if the burst generation mechanism is segregated to a dendritic compartment (as is likely, see Supplementary Figs 7,8), somatic current injections of the magnitude used in our experiments (0.5 nA) would cause large shifts in burst timing (~10-30ms) in a ramp-to-threshold network (see Supplementary Fig. 11).

While simplest hypothesis for the sequential activation of $HVC_{(RA)}$ neurons is that they are driven by sequential excitatory connections, we cannot rule out a role for other HVC neurons in this process. For example, $HVC_{(X)}$ neurons likely form synaptic connections onto $HVC_{(RA)}$ neurons [43], and with their stereotyped sparse bursting patterns, could contribute to the stereotyped pattern of subthreshold PSPs observed in $HVC_{(RA)}$ neurons. Similarly, HVC inhibitory neurons could contribute to the observed subthreshold PSPs, just as a decrease in inhibitory conductance could contribute to the large depolarization that precedes the onset of $HVC_{(RA)}$ bursts. To address these questions, experiments to analyze the excitatory and inhibitory conductances [50] will need to be carried out in the singing bird using intracellular recording techniques similar to those presented here.

Regardless of the neuron types involved, the subthreshold membrane potential fluctuations observed in $HVC_{(RA)}$ neurons give some clue to the network connectivity that could underlie a chain in HVC. In a 'perfect' chain, in which neurons effectively project only to subsequently active neurons (i.e. within the next 10ms), we would expect that a neuron would receive synaptic input only immediately prior to bursting. Thus, the presence of small stereotyped depolarizations throughout the song (between bursts) indicates that the HVC chain may be slightly 'noisy', containing deviations from perfect chain-like connectivity. However, given that single $HVC_{(RA)}$ neurons can produce EPSPs of up to 5mV on postsynaptic $HVC_{(RA)}$ neurons [43], the membrane potential fluctuations we observe could result from a relatively small numbers of imperfect connections. Given the possible role of spatial convergence on dendrites in the initiation of dendritic calcium spikes [51,52], the safety factor against erroneous burst generation could be much higher than suggested by the size of these subthreshold PSPs.

Our findings also suggest that the unitary event - or 'tick' - of this clock is a calcium spike in a small ensemble of HVC neurons. In the same way that sodium spikes tend to appear as all-or-none events with a fixed amplitude and temporal profile, calcium spikes tend to produce a stereotyped response to super-threshold inputs, even if these inputs have large variations in amplitude and temporal structure [19,53]. This regularization of the $HVC_{(RA)}$ burst has several beneficial effects on network behaviour, preventing the runaway growth or decay of activity during propagation, as well as making the network less sensitive

to noise. It also allows the network to function over a wide range of synaptic connection strengths and connectivity (Fig. 5)

Estimate of timing precision in HVC activity

Sequential activity in HVC has several striking properties: 1) Propagation is stable such that bursts do not grow or decay during the song, but are of a consistent size throughout the song motif [13]. 2) The bursts are locked to the song with sub-millisecond temporal precision and are nearly identical on every rendition of the song [54], and 3) Trial-to-trial variations in the speed of the sequential activity is in the range of 1-2%, based on variability in song timing [55]. However, measurements of timing precision based on acoustic signals are likely to be an underestimate of the underlying neuronal timing precision because they suffer from the inherent variability introduced by the vocal apparatus, and the fact that acoustic features exhibit modulations that are much slower than the rapid and stereotyped modulations that occur in the firing patterns of HVC and RA neurons [11,13,14]. An alternative approach is to analyze the jitter in the timing between the bursts of RA neurons, from which we can infer the timing precision in HVC activity. Such an analysis was carried out to examine the timing jitter between bursts of simultaneously recorded neurons in RA [14]. Neuron pairs (n=13) were analyzed in two birds. It was found that the jitter between individual identified RA bursts increased linearly between 20ms up to 400ms with a slope of 0.0074 in Bird 9, and a slope of 0.0071 in Bird 12. These numbers correspond to a timing CV of 0.74% and 0.71%, respectively. Note that this is likely to be an overestimate of the 'runtime jitter' inherent in the HVC chain because it includes slow changes in song tempo that can occur over the duration of the neuronal recording. Thus we estimate that the 'true' HVC runtime jitter is likely to be less than 0.75% over the timescale of a song syllable.

SUPPLEMENTAL REFERENCES

47. Nixdorf, B. E., Davis, S. S. & DeVoogd, T. J. Morphology of Golgi-impregnated neurons in hyperstriatum ventralis, pars caudalis in adult male and female canaries. J Comp Neurol 284, 337-49 (1989).

48. Fortune, E. S. & Margoliash, D. Parallel pathways and convergence onto HVc and adjacent neostriatum of adult zebra finches (Taeniopygia guttata). J Comp Neurol 360, 413-41 (1995).

49. Golomb, D., Yue, C. & Yaari, Y. Contribution of persistent Na+ current and M-type K+ current to somatic bursting in CA1 pyramidal cells: combined experimental and modeling study. J Neurophysiol 96, 1912-26 (2006).

50 Rudolph, M., Pospischil, M., Timofeev, I. & Destexhe, A. Inhibition determines membrane potential dynamics and controls action potential generation in awake and sleeping cat cortex. *J Neurosci* **27**, 5280-5290 (2007).

51 Williams, S. R. & Stuart, G. J. Dependence of EPSP efficacy on synapse location in neocortical pyramidal neurons. *Science* **295**, 1907-1910 (2002).

52 Westenbroek, R. E., Ahlijanian, M. K. & Catterall, W. A. Clustering of L-type Ca2+ channels at the base of major dendrites in hippocampal pyramidal neurons. *Nature* **347**, 281-284 (1990).

53 Lisman, J. E. Bursts as a unit of neural information: making unreliable synapses reliable. *Trends Neurosci* **20**, 38-43 (1997).

54 Chi, Z. & Margoliash, D. Temporal precision and temporal drift in brain and behavior of zebra finch song. *Neuron* **32**, 899-910 (2001).

55 Glaze, C. M. & Troyer, T. W. Temporal structure in zebra finch song: implications for motor coding. *J Neurosci* **26**, 991-1005 (2006).

Metric	Non-bursting	Bursting
Group width SD (ms)	3.617±1.696	1.175±0.3276
Group Latency SD (ms)	0.5979±0.1486	0.2619±0.06826
Mean number of spikes	6.745±1.837	4.579±0.2843
Mean spike number SD	2.28±1.098	0.6744±0.3841
Burst duration (ms)	11.61±4.404	5.77±0.08228
Run time jitter (%)	1.949±1.377	0.522±0.1714
Unreliability Index	0.2463±0.1221	0.1085±0.1329

Numbers expressed as mean±standard deviation.

Measurements are given of several metrics of network performance for comparison of non-bursting and bursting models. The standard deviation of the metrics is included as a measure of the variation of performance with changes in model parameters. The standard deviation (as well as the mean) of each metric were computed across networks over a range of excitatory synaptic conductances ($G_{EE\,\max}$ = 0.2 to 4 mS/cm^2 in intervals of 0.2 mS/cm^2) and connection probability values (P = 0.1, 0.2, 0.5, 1.0). Only networks that exhibited stable propagation were included in this analysis. For a description of the metrics used, see Supplementary Methods.

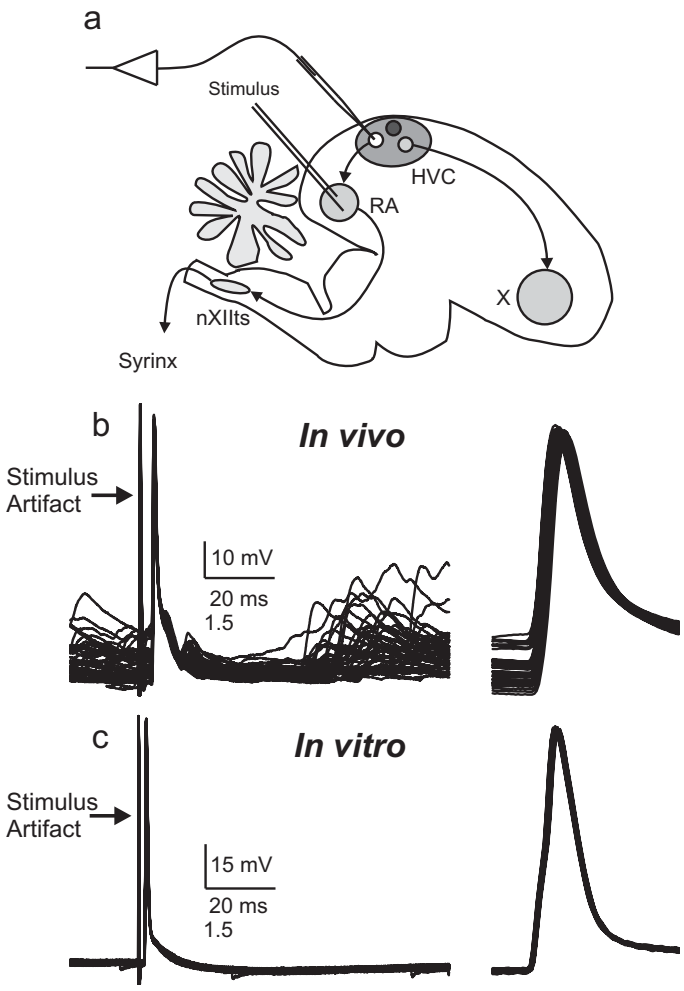

Supplementary Figure 1 – Antidromic identification of $HVC_{(RA)}$ neurons. a, Nucleus HVC has three major cell types, defined by their projections. To identify the neurons that project to RA, a bipolar stimulating electrode was inserted into RA and responses were recorded in HVC. Antidromic responses (b) *in vivo* and (c) *in vitro* showed short latency spiking responses to RA stimulation (<10ms) with minimal latency variability (<100μs RMS). A closer view of the spiking response is shown on the right. An overlay of 40 traces is given for each example neuron. Note that the antidromically-activated spikes rise from the resting potential without a preceding EPSP.

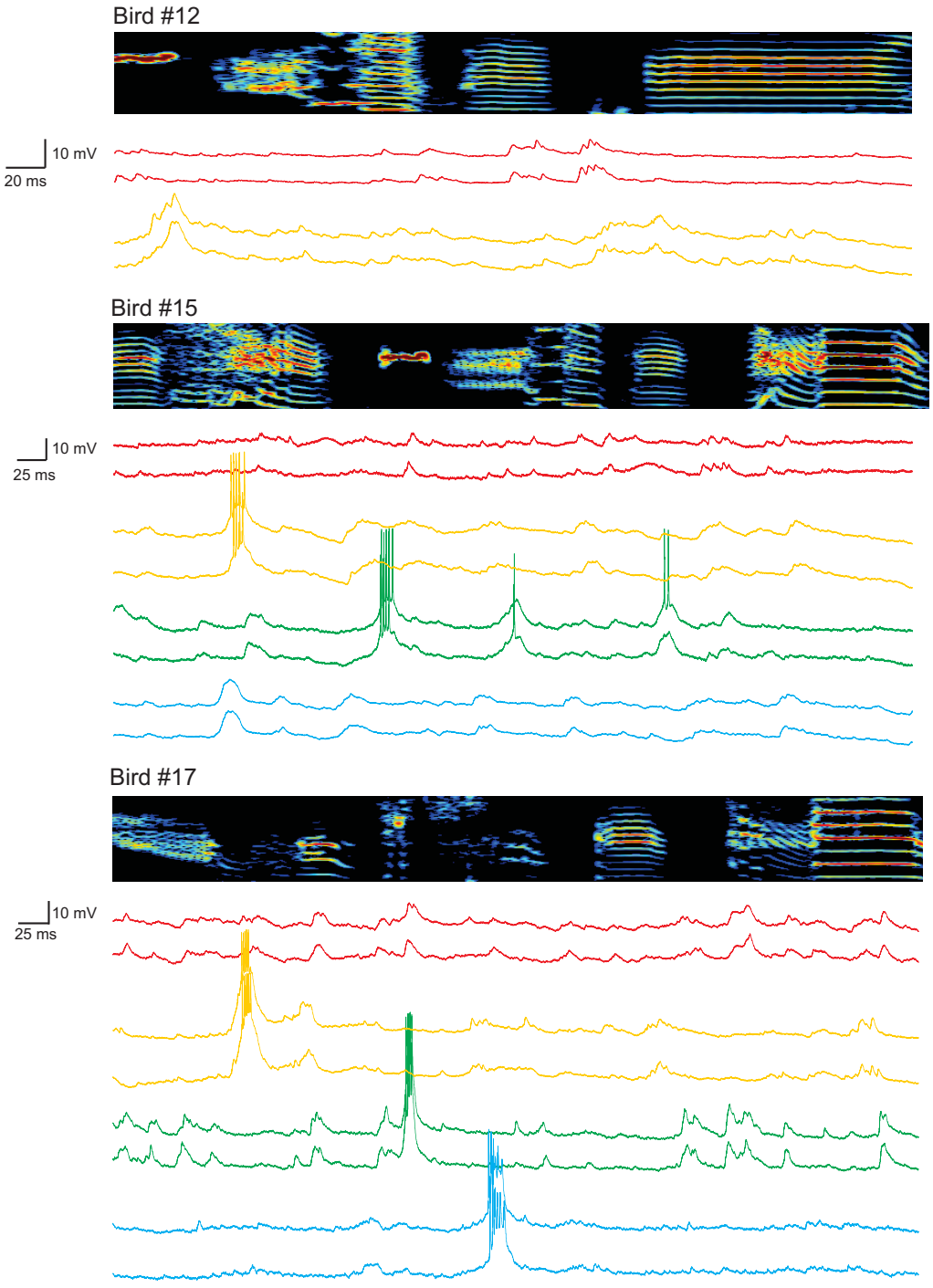

Supplementary Figure 2 – Examples of $HVC_{(RA)}$ membrane potential from multiple neurons in the same bird. There were three birds (#12, #15, #17) for which multiple neurons were recorded in the same animal. Shown are recordings from 10 neurons in these birds. For each neuron, the membrane potential is shown for two renditions of the song (same colour traces) plotted against a single representative sonogram. Within neurons, the song-aligned subthreshold fluctuations were highly correlated across song motifs, both for neurons that spike during singing (cross correlation 0.80±0.03, ± s.e.m. $p<10^{-9}$, n=7

neurons), and neurons that did not spike (cross correlation 0.81±0.07, $p<10^{-9}$, n=6 neurons). Note that across different neurons in the same animal, the subthreshold membrane potential is not significantly correlated (cross correlation 0.11±0.08, p>0.3, n=13 pairwise comparisons). This lack of correlation suggests that subthreshold membrane potential fluctuations are not driven by a global input from nuclei afferent to HVC, such as Uvaeformis (Uva) or nucleus interface (NIf).

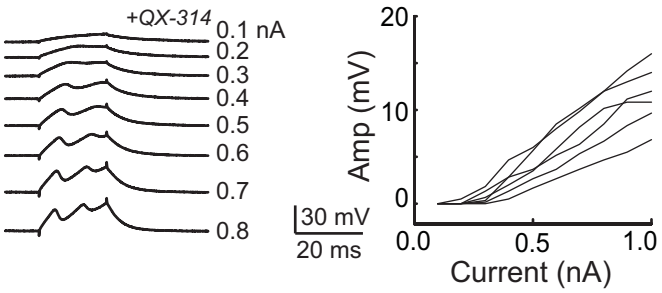

Supplementary Figure 3 – Electrophysiological properties of RA neurons in QX-314. As previously described, RA neurons generated evoked oscillations (left) with an amplitude and frequency that scaled with the magnitude of injected current [39]. Across the population of RA neurons recorded (right), the amplitude of evoked oscillations increased linearly with injected current. Note that the amplitude was defined as the difference between the initial depolarizing peak and the subsequent hyperpolarizing dip.

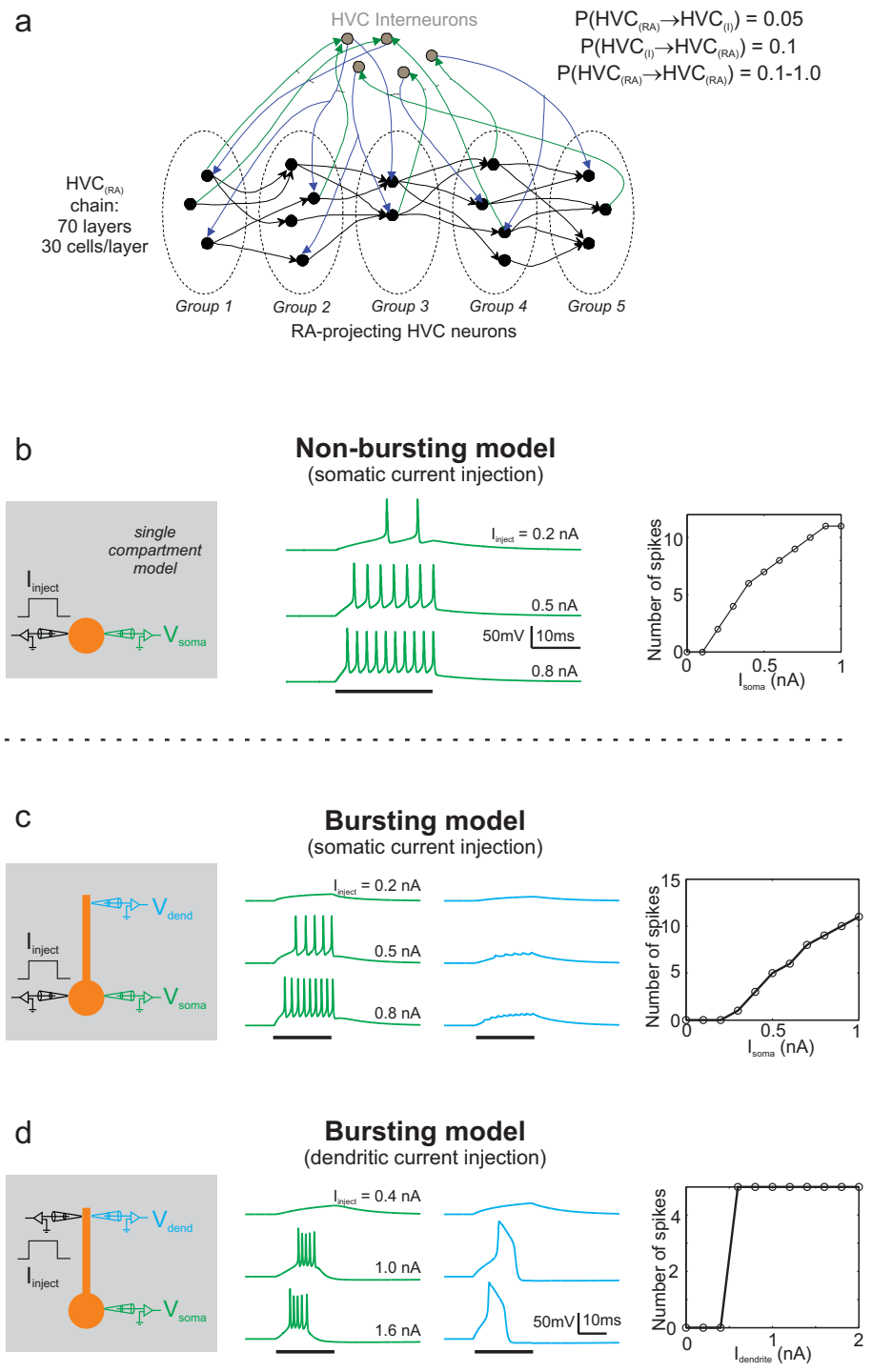

Supplementary Figure 4 – (Model result) A computational model of sequence generation in HVC. a) The network consisted of 70 groups of excitatory $HVC_{(RA)}$ neurons, each group containing 30 neurons. The excitatory neurons interacted with a population of 300 inhibitory interneurons, $HVC_{(I)}$. b) The non-bursting neuron was described by a single-compartment spiking model with sodium, potassium and leak conductances. Mathematical details of the network and neuronal models are given in Supplementary

Methods. Current pulses injected into the soma of the single-compartment model produced a graded response; larger currents resulted in a gradually increasing number of spikes (right). c) Current injections in the somatic compartment of the bursting neuron produced a graded spiking response with gradually increasing number of spikes at larger currents (right panel). Somatic current injection did not elicit a calcium spike in the dendritic compartment. d) In contrast, current injection into the dendrite elicited an all-or-none calcium spike, producing a stereotyped burst response in the soma. The result was a fixed number of spikes for above-threshold levels of current injection (compare to Figure 4c).

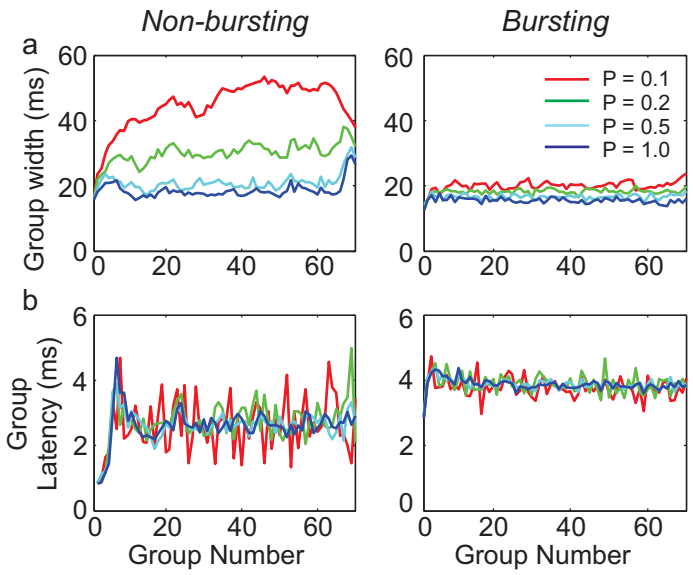

Supplementary Figure 5 - (Model result) Comparison of activity propagation in a chain network with non-bursting neurons (left panels) and bursting neurons (right panels). a) The average width of the burst of activity in a group of $HVC_{(RA)}$ neurons ('group width') is plotted as a function of group number (i.e. position along the chain). The x-axis also corresponds to time because the groups are active sequentially. For the non-bursting model, group width shows substantial time-dependence and sensitivity to $HVC_{(RA)}$ connection probability (P=0.1, 0.2, 0.5, and 1.0) (calculated at a $G_{EE\,\max}$ = 3 mS/cm^2). b) The average latency from one group to the next ('group latency') is plotted as a function of group number. For the non- bursting model, the group latency is variable and strongly time-dependent. In contrast, the bursting model shows no time-dependence and less variability in both group width and group latency. For more information about these measures, see Methods and Supplementary Methods. Quantitative measures of these results are provided in the Supplementary Table.

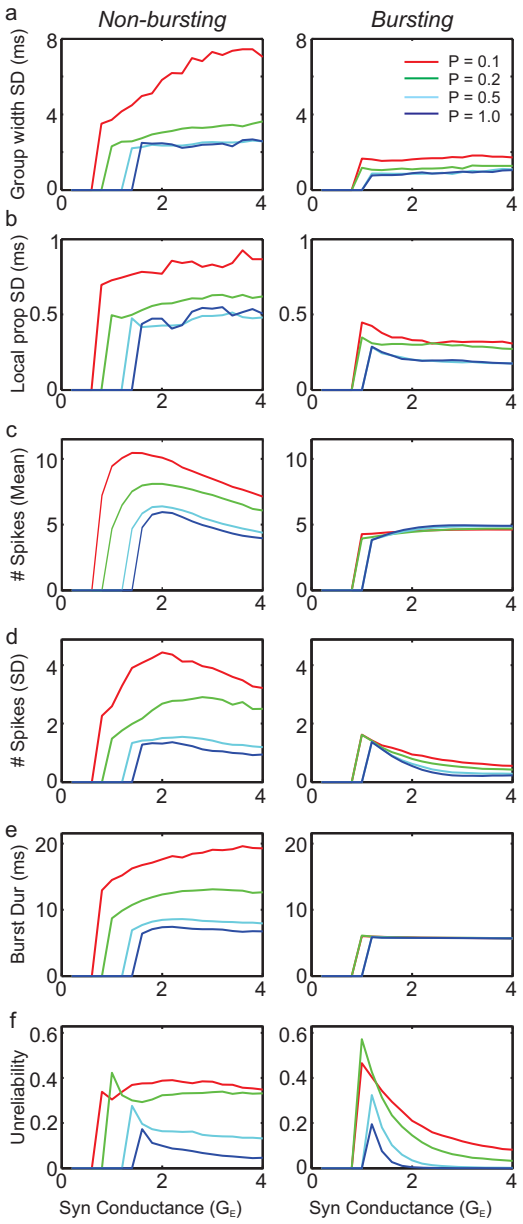

Supplementary Figure 6 – (Model result) Comparison of network performance of non-bursting and bursting models (left and right panels, respectively), over a range of connection probabilities and excitatory connection strengths. Comparison is made with regards to a) the standard deviation of group activity width (in milliseconds), b) the standard deviation of local propagation time (in milliseconds), c) the mean number of spikes per burst, d) the standard deviation of the number of spikes per burst, e) the burst duration (in milliseconds), f) and unreliability. For more information about these measures, see Methods and Supplementary Methods. Quantitative measures of these results are provided in the Supplementary Table.

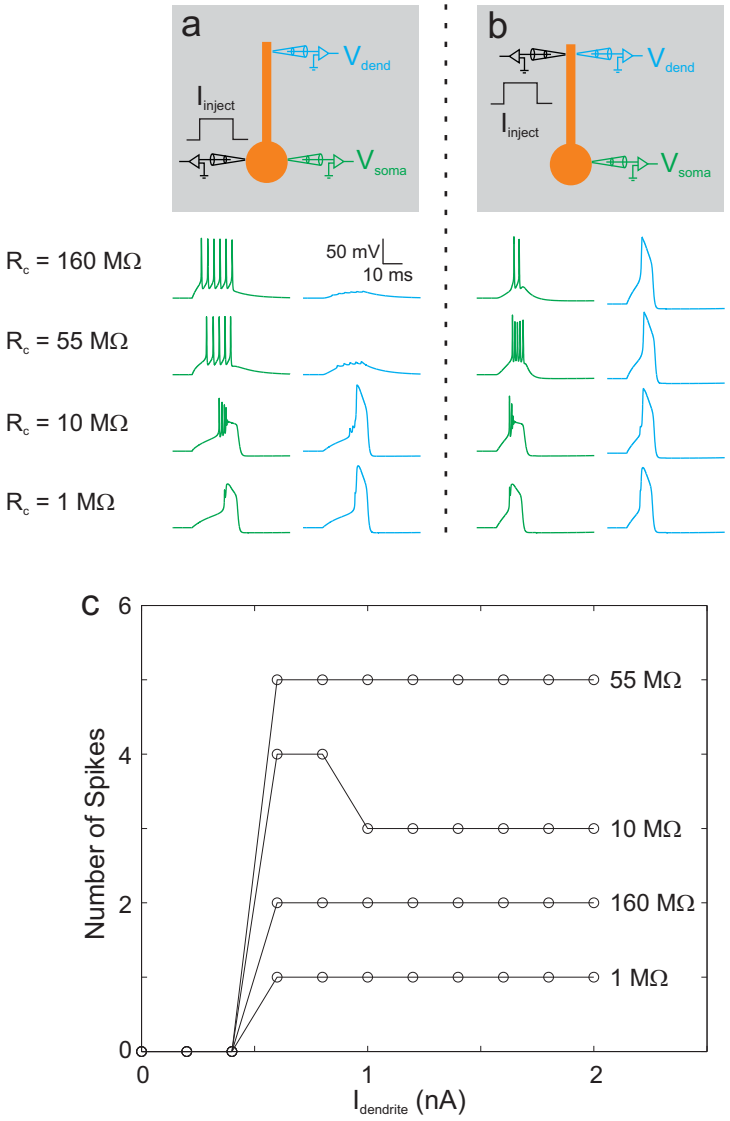

Supplementary Figure 7 – (Model result) Effect of systematic changes of the somato-dendritic coupling resistance (R_c). The coupling resistance is systematically varied from high to low values (R_c = 160, 55, 10, 1 MΩ) and the response of the neuron to injected somatic current (0.5nA, panel a) or dendritic current (1.0 nA, panel b) is examined. Somatic membrane potential traces are plotted in green; dendritic traces are shown in blue. At high values of R_c, somatic current injection elicits somatic spikes but does not elicit a dendritic calcium spike. In contrast, denritic current injection elicits a dendritic calcium spike, which drives current into the soma and generates a burst of sodium spikes. At sufficiently low values of R_c, the soma and dendrite are tightly coupled. Both somatic and dendritic current injections elicit a dendritic calcium spike, which drives current into the soma. However, the large depolarizing potential produces sodium channel inactivation and depolarization blockade of sodium spiking.

Intracellular recordings of $HVC_{(RA)}$ neurons during singing (Fig. 3 and Supplementary Fig. 2) show a strong underlying depolarizing event during bursts, but little evidence of profound sodium channel inactivation, which is not consistent with the firing patterns seen at the lower coupling resistances (R_c = 1 and 10 MΩ). Previous extracellular recordings [13] showed that $HVC_{(RA)}$ neurons generate 4-5 spikes per burst during singing, inconsistent with the higher coupling resistances (R_c >100MΩ). Therefore, we have modeled the two-compartment $HVC_{(RA)}$ neurons with Rc = 55mΩ.

c) All four of these models produce an all-or-none spiking response, because dendritic current injection in all of these models elicits a stereotyped calcium spike.

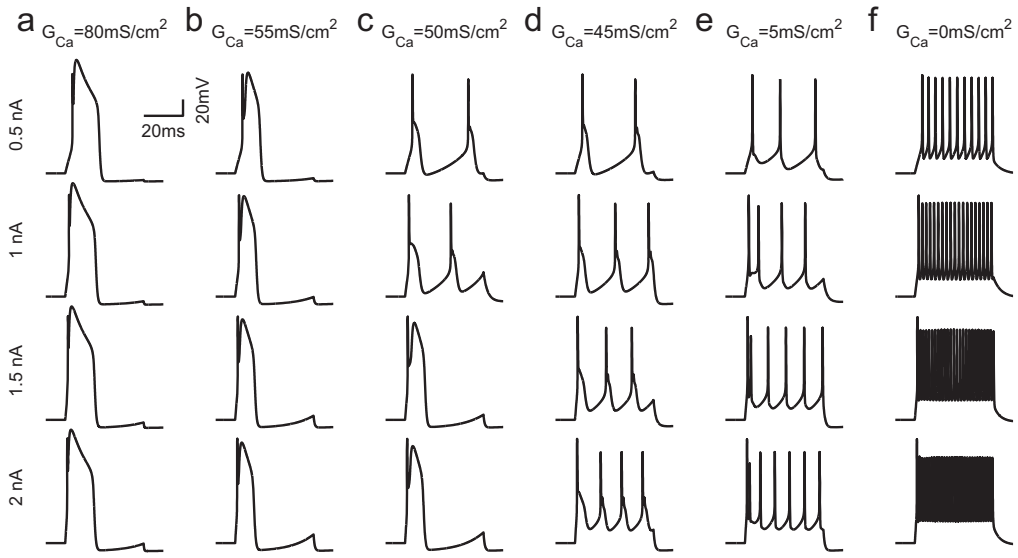

Supplementary Figure 8 – (Model result) Can a single-compartment model generate $HVC_{(RA)}$-like bursts? Shown are voltage traces from six different single-compartment models with varying amounts of high-threshold calcium conductance (a-f). The stimulus is a pulse current injection (50 ms duration) at four current levels (0.5, 1.0, 1.5, and 2.0 nA). The calcium conductances are: a) 80mS/cm^2; b) 55mS/cm^2; c) 50 mS/cm^2; d) 45mS/cm^2; e) 5 mS/cm^2; f) 0mS/cm^2 . The calcium-dependent potassium conductance that terminates the burst is maintained at 100 mS/cm^2. At high levels of calcium conductance (a and b) supra-threshold current injection elicits a large calcium-mediated plateau potential. There are no sodium spikes, due to rapid inactivation of the sodium conductance. At intermediate values of calcium conductance, high currents elicit calcium spikes, but low currents elicit single sodium spikes riding on depolarizing calcium transients that are subthreshold for the generation of a calcium spike. Finally, at lower levels of calcium conductance, the neuron generates (f) regular trains of sodium spikes, or (e) spike trains that exhibit spike-frequency adaptation due to the activation of the Ca-activated potassium channels. Because the sodium spike mechanism and the high-threshold calcium spike mechanism interfere with each other in a single-compartment, there is no regime in which the neuron can generate sodium spikes riding on a regenerative calcium spike event. In contrast, in the two-compartment model, the calcium currents are segregated to a separate dendritic compartment (Supplementary Fig. 4). In this case, the dendrite can exhibit a large calcium spike, driving current into the soma, which is free to generate a high-frequency burst of sodium spikes.

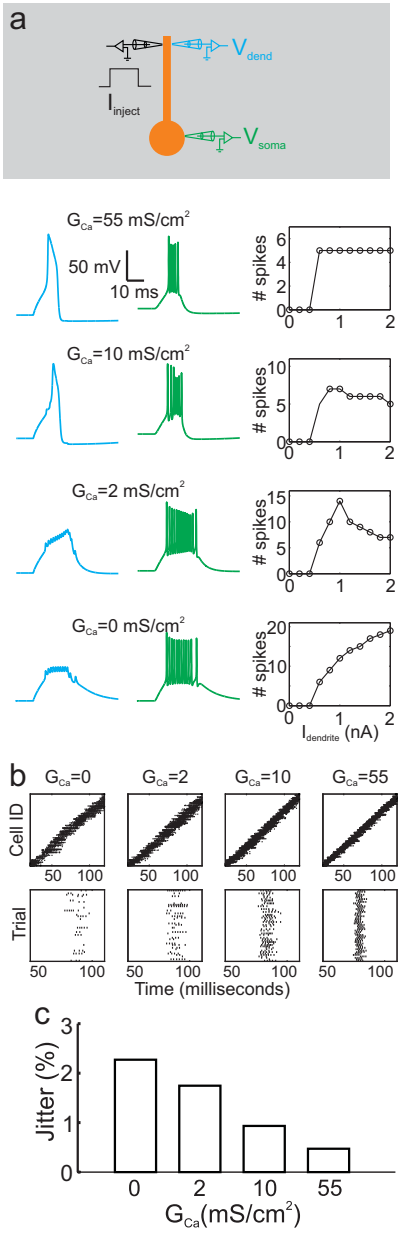

Supplementary Figure 9 – (Model result) Examination of timing jitter in a chain network with neurons varying continuously from non-bursting to bursting. Four two-compartment neuron models are compared with a range of dendritic calcium conductance G_{Ca} to produce different degrees of burstiness, ranging from the original fully bursting model in the main text ($G_{Ca} = 55$ mS/cm^2, top traces) to the non-bursting model with a passive dendrite ($G_{Ca} = 0$ mS/cm^2, bottom traces). For each model with non-zero

calcium conductance, the dendritic calcium-dependent potassium conductance G_{CaK} was increased to achieve a reasonable burst response to a dendritic calcium spike with minimal sodium channel inactivation. Dendro-somatic coupling resistance (R_c) was adjusted to achieve a somatic excitability that resulted in a network propagation speed the same as for the full bursting model (Fig 5b) at a synaptic strength of $G_{EE\max} = 3$ mS/cm^2. These constraints resulted in the following values for the four neuronal models: Model 1) $G_{Ca} = 55$, $G_{CaK} = 150$, and $R_C = 55$, Model 2) $G_{Ca} = 10$, $G_{CaK} = 40$, and $R_C = 30$, Model 3) $G_{Ca} = 2$, $G_{CaK} = 20$, and $R_C = 16$, and Model 4) $G_{Ca} = 55$, $G_{CaK} = 150$, and $R_C = 55$ respectively. Conductances have units of mS/cm^2; coupling resistance has units of MΩ. The inhibitory conductance onto the dendrite had to be slightly increased for networks with reduced calcium models, in order to limit burst broadening (runaway excitation). For models with a calcium conductance of 0, 2, 10, and 55 mS/cm2, the maximum inhibitory synaptic conductances on the dendrite were set to the following values, respectively: 0.7, 0.6, 0.3, 0.2 mS/cm^2.

a) Membrane potential traces of the dendrite (blue) and soma (green) under a pulse of current injection (20 ms, 1 nA) to the dendrite are shown. The number of spikes as a function of the injected current is plotted for each model (right panel). For the neurons with reduced calcium (2mS/cm^2), strong injected currents elicit a calcium spike and a stereotypical burst in the soma, but at low current values, the neuron exhibited a graded response with a more linear initial portion of the I-f curve. b) Simulation of the chain network using 2100 neurons (70 groups of 30 cells) over 50 trials with a connection probability $P = 0.1$. Shown are raster plots representing the first 120ms of the simulation (top) and a raster plot of 50 trials of a neuron in the 56th group (bottom). c) The runtime jitter of the four model networks (shown in panel b). The non-bursting model is the least reliable and an increasing contribution of intrinsic bursting leads to decreased runtime jitter.

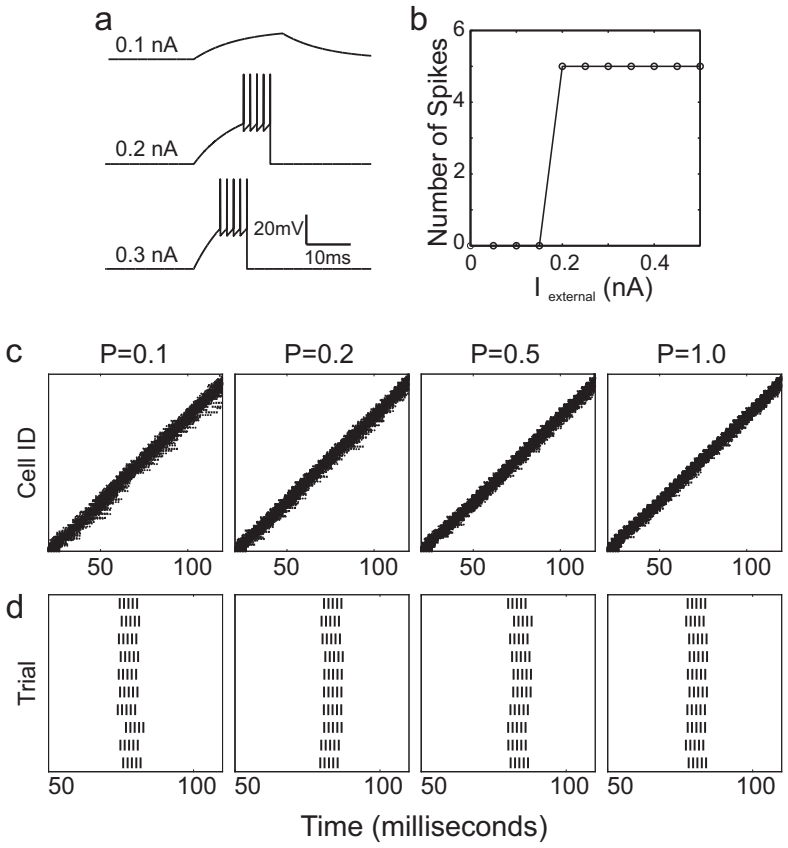

Supplementary Figure 10 – (Model result) A chain model with an integrate-and-burst neuron can also generate low temporal jitter. a) An integrate-and-burst neuron is just like an integrate-and-fire neuron, except that it generates a burst rather than a spike upon reaching threshold. The neuron has a single capacitive electrical compartment and a leak conductance, producing a membrane time constant of 10ms (the same as the non-bursting $HVC_{(RA)}$ model neuron in Supplementary Fig. 4b, see Supplementary Methods). b) The neuron exhibits an all-or-none burst response above threshold. c) A chain network (Supplementary Fig. 4a) was implemented with an integrate-and-burst model for $HVC_{(RA)}$ neurons and was tested for four different values of network connectivity (p=0.1, 0.2, 0.5 and 1.0). The runtime jitter of the integrate-and-burst network was very low (0.64± 0.09%, mean±S.D., averaged across the four network connectivities shown), comparable to the performance of the full two-compartment model of $HVC_{(RA)}$ neurons (Fig. 5f). This finding suggests that the stabilization of propagation of activity and reduction of timing jitter can be obtained using a simple intrinsic all-or-none bursting mechanism, regardless of the underlying biophysical mechanism.

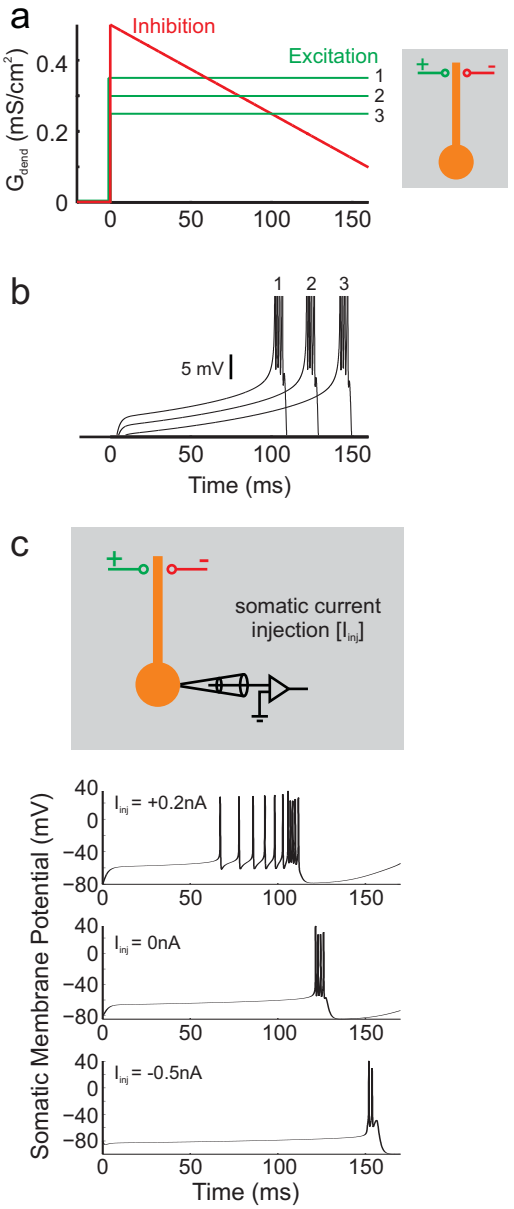

Supplementary Figure 11 - (Model result) Behaviour of a two-compartment $HVC_{(RA)}$ model neuron in a hypothetical ramp-to-threshold sequence generating circuit. The ramp-to-threshold circuit shown in Fig 1b was implemented using an $HVC_{(RA)}$ neuron that bursts via a dendritic calcium spike. We use the two-compartment model neurons described in Supplementary Methods (with the slight modification of a constant somatic inhibition of 0.2 mS/cm^2), a) A decreasing ramp of inhibitory conductance (red trace, from 0.5 mS/cm^2 to zero over a period of 200 ms) is applied to the dendrite. A step of constant excitatory conductance (green traces) is simultaneously applied, starting at time zero. b) Shown is the resulting

somatic membrane potential (black trace), which exhibits a slow depolarization until the activation of the dendritic calcium spike, at which point the neuron bursts. In the ramp-to-threshold model, three different neurons will burst sequentially if they are given three different constant levels of excitatory conductance (neurons 1,2 and 3 have excitatory conductance of 0.35, 0.3, 0.25 mS/cm^2, respectively). c) As described in the text, one prediction of the ramp-to-threshold model is that depolarizing current injected into the neuron would cause the burst to occur earlier. We wondered whether this prediction holds for somatic current injection in a neuron with a dendritic burst generating mechanism. For the model neuron '2' (0.3 mS/cm^2 constant excitatory conductance), depolarizing current injection of 0.2nA caused an advance of the burst timing by -15ms, whereas a hyperpolarizing current injection of -0.5nA caused a delay of the burst by +29ms. We also examined the change in burst timing for a higher value of the dendro-somatic coupling resistance (R_c=160MOhm, see Supplementary Fig 7); the same values of somatic current injection still produced easily detectable changes in burst timing (-7ms and +15ms, respectively).